



# Joint ptycho-tomography reconstruction through alternating direction method of multipliers

SELIN ASLAN,<sup>1</sup> VIKTOR NIKITIN,<sup>1,2</sup> DANIEL J. CHING,<sup>1</sup> TEKIN BICER,<sup>1,3</sup> SVEN LEYFFER,<sup>4</sup> AND DOĞA GÜRSOY<sup>1,5,\*</sup>

<sup>1</sup>X-ray Science Division, Argonne National Laboratory, 9700 Cass Avenue, Lemont, Illinois 60439, USA

<sup>2</sup>Max IV Laboratory, Fotongatan 2, 225 92 Lund, Sweden

<sup>3</sup>Data Science and Learning Division, Argonne National Laboratory, 9700 Cass Avenue, Lemont, Illinois 60439, USA

<sup>4</sup>Mathematics and Computer Science Division, Argonne National Laboratory, 9700 Cass Avenue, Lemont, Illinois 60439, USA

<sup>5</sup>Department of Electrical Engineering and Computer Science, Northwestern University, 2145 Sheridan Road, Evanston, Illinois 60208, USA

\*[dgursoy@anl.gov](mailto:dgursoy@anl.gov)

**Abstract:** We present the extension of ptychography for three-dimensional object reconstruction in a tomography setting. We describe the alternating direction method of multipliers (ADMM) as a generic reconstruction framework to efficiently solve the nonlinear optimization problem. In this framework, the ADMM breaks the joint reconstruction problem into two well-defined subproblems: ptychographic phase retrieval and tomographic reconstruction. In this paper, we use the gradient descent algorithm to solve both problems and demonstrate the efficiency of the proposed approach through numerical simulations. Further, we show that the proposed joint approach relaxes existing requirements for lateral probe overlap in conventional ptychography. Thus, it can allow more flexible data acquisition.

© 2019 Optical Society of America under the terms of the [OSA Open Access Publishing Agreement](#)

## 1. Introduction

Ptychography is an emerging coherent diffraction imaging (CDI) technique that can provide a spatial resolution much finer than the illuminating beam's size, thus overcoming the resolution limitations of traditional lens-based microscopy [1]. It uses a focused beam of light for scanning the object in a series of overlapping positions while collecting far-field diffraction patterns at each illumination position (Fig. 1, [2]). In this way, objects larger than the beam size can be imaged at high resolution by combining the principles of scanning-probe microscopy with CDI. Following initial experimental demonstrations [3–6], implementations of ptychographic systems at synchrotrons today can create three-dimensional images [7–9] of a range of samples from biology [10–14] to materials sciences [15–26], and the technique is becoming the standard method for sub-20 nm x-ray imaging [27].

Current algorithmic efforts in ptychography are mostly for 2D imaging and are based on the solution of the phase retrieval problem [28–45]. For 3D imaging, phase retrieval problems are solved independently for each view of the object around a common rotation axis, followed by a 3D tomographic reconstruction. This sequential or two-step reconstruction approach imposes rigid constraints on data collection, such as lateral probe overlap, and is not suitable for sparse or compressed sampling of data to improve the acquisition times. However, because all measurements in a tomography setting retain partial information about the object to be recovered, solving ptychography and tomography problems jointly enables relaxing these rigid constraints and can allow for rapid scanning of large volumes more efficiently by using the intrinsic coupling of information among projections [2]. In addition, regularization of the joint problem based

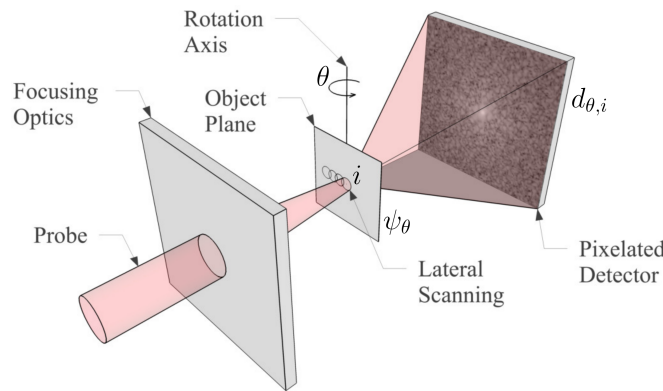


Fig. 1. Layout of a ptychographic data collection setup [2]. An object is raster-scanned with a finite-extent coherent beam (painted in pink) to obtain a set of diffraction data recorded by a pixelated detector located downstream of the object. A full tomography dataset can be obtained by repeating the planar scanning process for different angular positions of the object around a vertical rotation axis.

on prior information about the object can improve the conditioning of both problems and yield improved reconstructions.

There have been recent studies on jointly solving the ptycho-tomography problem. In [2], the object is recovered using the alternating minimization approach by coupling ptychographic phase retrieval and tomography problem using two different cost functions. On the other hand, in [46], authors solve the joint problem based on a single optimization cost-function. Another related approach is multi-slice ptychographic tomography for 3D imaging, which enables recovering thick objects [47–50].

In this paper, we extend the alternating minimization approach introduced in [2] and propose the alternating direction method of multipliers (ADMM) [51] as a generic reconstruction framework for solving the joint ptycho-tomography problem. In our proposed ADMM framework, we break the joint reconstruction problem into two well-defined subproblems: ptychographic phase retrieval and tomographic reconstruction. The main difference between these two approaches is that ADMM framework introduces a dual variable which connects the two minimization problems. Note that [2] uses a single step of each minimization in an alternating fashion to update the object without directly connecting the two subproblems. Moreover, since we minimize the augmented Lagrangian by separating the minimization over two variables in ADMM, each minimization problem is also different than the ones in [2] as we explain in more details in Section 2.

ADMM was first introduced in [52,53] and is closely related to dual decomposition, the method of multipliers, Douglas-Rachford splitting, Dykstra's alternating projections, and proximal methods (see [51] and references therein). The method has been widely used for convex optimization, and its convergence has been analyzed for both convex and nonconvex optimization problems [54–57]. In our study, we use the gradient descent algorithm to solve each problem, but the framework allows us to use other optimizers and regularization methods for each subproblem. We discuss its convergence behavior and analyze reconstruction quality in comparison with other methods.

## 2. Methods

In this section, we present the mathematical model for the joint ptycho-tomography problem and define its augmented Lagrangian formulation. Furthermore, we state the optimality conditions

for our approach.

### 2.1. Mathematical model

We can define the joint ptycho-tomography problem for reconstructing the complex refractive index distribution of a 3D object,  $x$ , from its intensity or amplitude measurements at the far plane. Since an amplitude-based cost function is computationally more efficient [58, 59], we aim to minimize the difference between the estimated and the measured amplitudes of the wave on the detector plane as

$$\min_x \frac{1}{2} \sum_{\theta=1}^M \sum_{i=1}^N \|f_{\theta,i}(x) - d_{\theta,i}\|_2^2, \quad (1)$$

where  $i$  is the position index at object rotation angle  $\theta$ ,  $N$  is the number of images collected for each rotation,  $M$  is the total number of rotations performed,  $f$  is the forward operator that maps  $x$  onto measurements, and  $d_{\theta,i}$  are the measurement vectors. Note that  $\theta$  and  $i$  are indices used to define the geometry of each illumination probe, not variables.

In this paper, however, we consider an alternative form by splitting the tomography and ptychography problems and reformulating (1) into a consensus form by introducing a set of constraints based on tomography equations. Let  $f_{\theta,i}(x) = g_i(h_{\theta}(x))$ , where  $g_i(\psi_{\theta}) = |FQ_i\psi_{\theta}|$  and  $h_{\theta}(x)$  are the object-to-detector plane wave propagation and projection forward operators in ptychography and tomography, respectively. Then, we obtain

$$\min_{\psi_1, \dots, \psi_M} \sum_{\theta=1}^M \left( \frac{1}{2} \sum_{i=1}^N \|g_i(\psi_{\theta}) - d_{\theta,i}\|_2^2 \right), \quad (2)$$

$$\text{subject to } \psi_{\theta} = h_{\theta}(x), \quad \theta = 1, 2, \dots, M, \quad (3)$$

where  $\psi_{\theta}$  is the object transmission function for each rotation of the object by  $\theta$ . The term provided in parentheses represents a conventional phase retrieval data fidelity term for a specific rotation angle. The constraints in Eq. (3) for each view angle are to enforce that all tomographic projections are consistent for a given object. This allows us to split the ptychographic phase retrieval and tomography problems using the ADMM approach as described in the following section.

### 2.2. Augmented Lagrangian formulation

The augmented Lagrangian method [60–62] has been increasingly used for solving constrained optimization problems. The optimization problem in Eq. (2) with constraints from Eq. (3) can be solved by recasting it into an equivalent problem with complex augmented variables, see [63] for details. The augmented Lagrangian of the corresponding equivalent problem is defined for a positive penalty parameter,  $\rho$ , and a set of dual variables,  $\lambda_{\theta}$ , associated with each consensus constraint for Eq. (2), as follows

$$\begin{aligned} \mathcal{L}_{\rho}(\psi_1, \dots, \psi_M, x, \lambda_1, \dots, \lambda_M) = & \sum_{\theta=1}^M \left( \frac{1}{2} \sum_{i=1}^N \|g_i(\psi_{\theta}) - d_{\theta,i}\|_2^2 \right. \\ & \left. + 2\operatorname{Re}\{\lambda_{\theta}^*(\psi_{\theta} - h_{\theta}(x))\} + \rho\|\psi_{\theta} - h_{\theta}(x)\|_2^2 \right), \end{aligned} \quad (4)$$

where  $\lambda_\theta^*$  is the Hermitian conjugate of  $\lambda_\theta$ . The ADMM iterations for solving  $x$  and  $\psi_\theta$  for each rotation angle can then be expressed as

$$\psi_\theta^{k+1} = \arg \min_{\psi_\theta} \mathcal{L}_\rho \left( \psi_\theta, x^k, \lambda_\theta^k \right), \quad \theta = 1, 2, \dots, M, \quad (5)$$

$$x^{k+1} = \arg \min_x \mathcal{L}_\rho \left( \psi_1^{k+1}, \dots, \psi_M^{k+1}, x, \lambda_1^k, \dots, \lambda_M^k \right), \quad (6)$$

$$\lambda_\theta^{k+1} = \lambda_\theta^k + \rho \left( \psi_\theta^{k+1} - h_\theta(x^{k+1}) \right), \quad \theta = 1, 2, \dots, M, \quad (7)$$

where  $k$  is the iteration number. In each update of  $\psi_\theta$  and  $x$ ,  $\mathcal{L}_\rho$  is minimized over the corresponding variable, using the most recent value of the other variables. The dual variable is then updated based on the scaled sum of the consensus errors or the residual between the updates variables.

Explicitly deriving the update rules for the ADMM iterations using Eq. (4), we obtain the following two minimization problems and an update formula for the dual variable:

$$\psi_\theta^{k+1} = \arg \min_{\psi_\theta} \frac{1}{2} \sum_{i=1}^N \|g_i(\psi_\theta) - d_{\theta,i}\|_2^2 + \rho \|\psi_\theta - h_\theta(x^k) + \lambda_\theta^k / \rho\|_2^2, \quad \theta = 1, 2, \dots, M \quad (8)$$

$$x^{k+1} = \arg \min_x \sum_{\theta=1}^M \rho \|h_\theta(x) - \psi_\theta^{k+1} - \lambda_\theta^k / \rho\|_2^2, \quad (9)$$

$$\lambda_\theta^{k+1} = \lambda_\theta^k + \rho \left( \psi_\theta^{k+1} - h_\theta(x^{k+1}) \right), \quad \theta = 1, 2, \dots, M. \quad (10)$$

The minimization steps in Eq. (8) form a set of ptychographic phase retrieval problems that can be solved individually or in parallel. The second term on the right-hand side of Eq. (8) is treated as a regularization term for each ptychographic phase retrieval problem based on the current object estimate and is not available in the alternating minimization approach in [2]. Next, we solve the conventional tomographic reconstruction problem expressed in Eq. (9) and perform a dual variable update for each angle. Here,  $\lambda_\theta$ -update can be seen as an adjustment step for the algorithm which connects the two minimization steps in Eqs. (8) and (9).

### 2.3. Optimality conditions

To choose a reasonable termination criterion, we first state the Karush-Kuhn-Tucker (KKT) conditions of Eqs. (2) and (3):

$$0 = \psi_\theta - h_\theta(x), \quad \theta = 1, 2, \dots, M, \quad (11)$$

$$0 = \nabla_{\psi_\theta} \mathcal{L}_0(\psi_\theta, x, \lambda_\theta) = \frac{1}{2} \nabla_{\psi_\theta} \left( \sum_{i=1}^N \|g_i(\psi_\theta) - d_{\theta,i}\|_2^2 \right) + \lambda_\theta \quad \theta = 1, 2, \dots, M, \quad (12)$$

$$0 = \nabla_x \mathcal{L}_0(\psi_1, \dots, \psi_M, x, \lambda_1, \dots, \lambda_M) = -2 \sum_{\theta=1}^M \nabla_x \text{Re}\{h_\theta(x)\}^T \lambda_\theta, \quad (13)$$

where Eq. (11) is primal feasibility, Eqs. (12) and (13) are dual feasibility conditions. In the following, we assume that  $\psi_\theta^{k+1}$  and  $x^{k+1}$  are optimal solutions, which must satisfy the KKT conditions of their respective subproblems Eqs. (5) and (6). The gradient of  $\mathcal{L}_\rho$  with respect to the real and imaginary parts of  $\psi_\theta$  or  $x$  follow the  $\mathbb{CR}$ -calculus formalism [64, 65]; that is, we treat these variables and their complex conjugates as two independent variables.

Since  $\psi_\theta^{k+1}$  minimizes  $\mathcal{L}_\rho(\psi_\theta, x^k, \lambda_\theta^k)$ , its gradient must vanish at  $\psi_\theta^{k+1}$ . Hence, for each  $\theta$ , we have

$$0 = \frac{1}{2} \nabla_{\psi_\theta} \left( \sum_{i=1}^N \|g_i(\psi_\theta) - d_{\theta,i}\|_2^2 \right) + \rho \left( \psi_\theta^{k+1} - h_\theta(x^k) + \lambda_\theta^k / \rho \right) \quad (14)$$

$$= \frac{1}{2} \nabla_{\psi_\theta} \left( \sum_{i=1}^N \|g_i(\psi_\theta) - d_{\theta,i}\|_2^2 \right) + \lambda_\theta^{k+1} + \rho \left( h_\theta(x^{k+1}) - h_\theta(x^k) \right). \quad (15)$$

In order to satisfy the KKT condition in Eq. (12),  $\rho(h_\theta(x^{k+1}) - h_\theta(x^k))$  must vanish as well. Similarly, since  $x^{k+1}$  minimizes  $\mathcal{L}_\rho(\psi_1^{k+1}, \dots, \psi_M^{k+1}, x, \lambda_1^k, \dots, \lambda_M^k)$ , its gradient must vanish at  $x^{k+1}$ :

$$0 = \sum_{\theta=1}^M 2\rho \nabla_x \operatorname{Re}\{h_\theta(x^{k+1})\}^T \left( h_\theta(x^{k+1}) - \psi_\theta^{k+1} - \lambda_\theta^k / \rho \right) \quad (16)$$

$$= - \sum_{\theta=1}^M 2 \nabla_x \operatorname{Re}\{h_\theta(x^{k+1})\}^T \lambda_\theta^{k+1}. \quad (17)$$

Hence, it follows that Eq. (13) is always satisfied. Therefore, we can now define the primal and dual residuals,  $r_\theta^{k+1}$  and  $s_\theta^{k+1}$  respectively, as follows:

$$r_\theta^{k+1} = \psi_\theta^{k+1} - h_\theta(x^{k+1}), \quad \theta = 1, 2, \dots, M, \quad (18)$$

$$s_\theta^{k+1} = \rho \left( h_\theta(x^{k+1}) - h_\theta(x^k) \right), \quad \theta = 1, 2, \dots, M. \quad (19)$$

If we solve both problems approximately, however, we need to monitor the following set of residuals in addition to Eqs. (18) and (19):

$$s_2^{k+1} = \frac{1}{2} \nabla_{\psi_\theta} \left( \sum_{i=1}^N \|g_i(\psi_\theta) - d_{\theta,i}\|_2^2 \right) + \lambda_\theta^{k+1}, \quad \theta = 1, 2, \dots, M. \quad (20)$$

$$s_3^{k+1} = - \sum_{\theta=1}^M 2 \nabla_x \operatorname{Re}\{h_\theta(x^{k+1})\}^T \lambda_\theta^{k+1}, \quad (21)$$

Here, Eqs. (20) and (21) are nonzero residuals when an optimal solution is not reached in each of the subproblems. Hence, we stop when the following conditions hold:

$$\|r^k\|_2 \leq \epsilon^{\text{pri}}, \quad \text{and} \quad \|s^k\|_2 \leq \epsilon^{\text{dual}}, \quad \|s_2^k\|_2 \leq \epsilon^{\text{dual}_2}, \quad \text{and} \quad \|s_3^k\|_2 \leq \epsilon^{\text{dual}_3}, \quad (22)$$

where  $\epsilon^{\text{pri}}$ ,  $\epsilon^{\text{dual}}$ ,  $\epsilon^{\text{dual}_2}$ , and  $\epsilon^{\text{dual}_3}$  are the chosen tolerances; see [51]. In theory, ADMM converges very slowly to a high-accuracy solution. On the other hand, exact solutions to Eqs. (5) and (6) are not necessary for ADMM convergence and are often avoided in practice.

For a faster convergence rate, we can also vary the penalty parameter  $\rho$  following [51]

$$\rho^{k+1} = \begin{cases} \tau^{\text{incr}} \rho^k & \text{if } \|r^k\|_2 > \mu \|s^k\|_2 \\ \rho^k / \tau^{\text{decr}} & \text{if } \|s^k\|_2 > \mu \|r^k\|_2 \\ \rho^k & \text{otherwise,} \end{cases}$$

where  $\mu > 1$ ,  $\tau^{\text{incr}} > 1$  and  $\tau^{\text{decr}} > 1$  are parameters which ensure that the primal and dual residuals remain within a factor of  $\mu$  as they both converge to zero. As suggested in [51], we chose  $\mu = 10$  and  $\tau^{\text{incr}} = \tau^{\text{decr}} = 2$ . We discuss more implementation details in Section 3.

## 2.4. Solution of the ptychography problem

To solve individual ptychography problems as expressed in Eq. (8), we considered the gradient descent algorithm with the general form

$$\psi_\theta^{m+1} = \psi_\theta^m - \gamma \nabla_{\psi_\theta} \mathcal{L}_\rho(\psi_\theta, x^k, \lambda_\theta^k), \quad (23)$$

where  $m$  is the iteration number for the gradient descent algorithm,  $\nabla_{\psi_\theta} \mathcal{L}_\rho(\psi_\theta, x^k, \lambda_\theta^k)$  is the step direction, and  $\gamma$  is the step size.

Consider each diffraction measurement as

$$d_{\theta,i}^2 = |FQ_i\psi_\theta|^2, \quad (24)$$

where  $F$  is the matrix representation of a 2D discrete Fourier transform,  $Q_i$  is the incident illumination at position  $i$ , and  $\psi_\theta$  is the object transmission function for each rotation of the object by  $\theta$ . Sometimes  $Q_i$  is also unknown and needs to be reconstructed simultaneously with  $\psi_\theta$ . For simplicity, however, in this paper we will assume that it is known.

By explicitly writing the data formation process in Eq. (8), we can derive the gradient as in [58]:

$$\begin{aligned} \nabla_{\psi_\theta} \mathcal{L}_\rho(\psi_\theta, x^k, \lambda_\theta^k) &= \frac{1}{2} \sum_{i=1}^N \left( Q_i^* Q_i \psi_\theta - Q_i^* F^* \text{Diag} \left( \frac{FQ_i \psi_\theta}{|FQ_i \psi_\theta|} \right) d_{\theta,i} \right) \\ &\quad + \rho \left( \psi_\theta - h_\theta(x^k) + \lambda_\theta^k / \rho \right), \quad \theta = 1, 2, \dots, M, \end{aligned} \quad (25)$$

where  $Q^*$  and  $F^*$  are the Hermitian conjugates of  $Q$  and  $F$ . The update formula for the object-transmission function is then

$$\begin{aligned} \psi_\theta^{m+1} &= (1 - \gamma \rho) \psi_\theta^m + \gamma \rho \left( h_\theta(x^k) - \lambda_\theta^k / \rho \right) \\ &\quad - \frac{\gamma}{2} \sum_{i=1}^N Q_i^* \left( Q_i \psi_\theta^m - F^* \text{Diag} \left( \frac{FQ_i \psi_\theta^m}{|FQ_i \psi_\theta^m|} \right) d_{\theta,i} \right), \quad \theta = 1, 2, \dots, M. \end{aligned} \quad (26)$$

Note that this updating formula is identical to that used in the commonly known *error reduction* algorithm as  $\rho$  approaches zero.

## 2.5. Solution of the tomography problem

Consider the definition of  $h_\theta(x)$ :

$$h_\theta(x) = \exp \left( i \frac{2\pi}{\nu} R_\theta x \right), \quad (27)$$

where  $i$  is  $\sqrt{-1}$ ,  $\nu$  is the wavelength of the illumination beam,  $x$  is the unknown refractive index of the object.  $R_\theta$  is the projection matrix of the sizes  $K^2 \times K^3$ , where  $K$  is the object size in one dimension that maps  $x$  to its projection for a rotation angle  $\theta$ .

Often the nonlinear (logarithmic) relationship between the transmission wave and the object is avoided by a change of variables. Therefore, instead of solving Eq. (9), we replace the nonlinearity introduced by the exponential term in Eq. (27) and minimize the following function:

$$\min_x \sum_{\theta=1}^M \|R_\theta x - \phi_\theta\|_2^2, \quad (28)$$

where  $\phi_\theta = -\iota \frac{\nu}{2\pi} \log \left( \psi_\theta^{k+1} + \lambda_\theta^k / \rho \right)$  is introduced for brevity. Here, we assume that  $\psi_\theta$  takes the angle values in 0 to  $2\pi$  range. Note that for larger objects, phase unwrapping may be needed. In the following lemma, we state that under mild assumptions, solving Eqs. (9) and (28) is equivalent.

**Lemma 2.1** *Let  $\mathbf{R}$  be the projection matrix for all rotation angles,  $\theta = 1, 2, \dots, M$  and have full column rank. Assume that Eqs. (9) and (28) are solved to optimality. Then, Eq. (28) is equivalent to Eq. (9).*

*Proof:* Solving Eq. (28) to optimality implies the following first-order conditions:

$$\mathbf{R}^T \left( \mathbf{R}x + \iota \frac{\nu}{2\pi} \log \left( \psi^{k+1} + \lambda^k / \rho \right) \right) = 0. \quad (29)$$

Since we assume that  $\mathbf{R}$  has full column rank, it follows that

$$\left( \mathbf{R}x + \iota \frac{\nu}{2\pi} \log \left( \psi^{k+1} + \lambda^k / \rho \right) \right) = 0, \quad (30)$$

which is equivalent to the first-order optimality condition for solving Eq. (9), namely,

$$\exp \left( \iota \frac{2\pi}{\nu} \mathbf{R}x \right) - \psi^{k+1} - \lambda^k / \rho = 0. \quad (31)$$

□

Hence, we replace the ADMM iteration in Eq. (9) by its reformulation Eq. (28):

$$x^{k+1} = \arg \min_x \sum_{\theta=1}^M \| R_\theta x - \phi_\theta \|_2^2. \quad (32)$$

Because of the update in ADMM iterations, we use the optimality condition for solving Eq. (32) as a stopping criterion instead of Eq. (21):

$$s_3^{k+1} = \sum_{\theta=1}^M R_\theta^T (R_\theta x^{k+1} - \phi_\theta). \quad (33)$$

Similar to the solution of the ptychography problem, we use the gradient descent algorithm for the solution of the tomography problem Eq. (32). The iteration formula with a positive step size  $\eta$  is given by

$$x^{n+1} = x^n + \eta \sum_{\theta=1}^M R_\theta^T (\phi_\theta - R_\theta x^n), \quad (34)$$

For computing operators  $R_\theta$  and  $R_\theta^T$  for all angles simultaneously we use the Fourier-based method [66] that decreases total computational complexity from  $O(MK^3)$  to  $O(K^2 \log K + MK^2)$ , where  $M$  is the total number of angles, and  $K$  is the object size in one dimension.

In practice, ADMM implementations do not solve the  $\psi_\theta$  and  $x$  subproblems exactly [51]. Instead, both problems are solved approximately, which means that Lemma 2.1 no longer applies. In our numerical results below, however, we still observe convergence of the overall scheme. We are investigating the application of global convergence results for augmented Lagrangian methods to develop a formal mathematical proof of convergence for the case when the subproblems are approximately minimized, which we leave to a forthcoming paper.

The pseudo-code for the ADMM implementation is provided in Algorithm 1.

**Algorithm 1** Joint ptycho-tomography reconstruction via ADMM

---

```

Initialize  $\eta, \gamma, \rho, \psi_\theta^0, x^0, \lambda_\theta^0$ , and given  $Q = [Q_1^T Q_2^T \cdots Q_N^T]^T$ 
while not converged do
    for  $\theta = 1, \dots, M$  do
         $\psi_\theta^{k+1} \leftarrow \arg \min_{\psi_\theta} \frac{1}{2} \sum_{i=1}^N \|g_i(\psi_\theta) - d_{\theta,i}\|_2^2 + \rho \|\psi_\theta - h_\theta(x^k) + \lambda_\theta^k/\rho\|_2^2$  via Eq. (26)
    end for
     $x^{k+1} \leftarrow \arg \min_x \sum_{\theta=1}^M \|R_\theta x - \phi_\theta\|_2^2$  via Eq. (34)
    for  $\theta = 1, \dots, M$  do
         $\lambda_\theta^{k+1} = \lambda_\theta^k + \rho (\psi_\theta^{k+1} - h_\theta(x^{k+1}))$ 
    end for
     $k \leftarrow k + 1$ 
end while
Return  $x^k$ 

```

---

**3. Results**

Here, we demonstrate the efficiency of the ADMM algorithm through numerical simulations and discuss its convergence behavior.

**3.1. Simulation setup**

To evaluate the effectiveness of Algorithm 1, we perform numerical tests using a synthetic phantom. Our experimental setup is similar to the one in [2], where Fienup's error-reduction algorithm was extended to obtain a 3D object reconstruction from ptychographic data collected in a tomography setting. We used XDesign [67] to generate a discrete 3D object with a shape of  $64 \times 64 \times 64$  and a voxel size of 10 nm (Fig. 2a-b). The object is represented by its complex refractive index:  $x = \delta + i\beta$ , where  $1 - \delta$  and  $\beta$  are the decrement of the refractive index, related to the phase shift of the incident wave, and the absorption index, describing attenuation of the wave, respectively. We use an object that is made of two strongly absorbing materials, gold (Au) and platinum (Pt), and two weakly absorbing materials, zinc oxide (ZnO) and titanium dioxide ( $TiO_2$ ). The densities of these materials are 19.32, 21.45, 5.606, and 4.23 g/cm<sup>3</sup>, respectively. A circularly shaped probe function of 150 nm diameter (15 pixels) with a constant phase is used for the simulations throughout the paper. The distance between adjacent probe center positions are set to 40 nm and 100 nm (4 and 10 pixels) that approximately correspond to 70% and 30% overlap, respectively. Far-field diffraction patterns are recorded by a  $63 \times 63$  pixelated detector. In Figure 2c, we show the simulated measurement data with and without applying Poisson noise with the square-root of the corresponding peak intensity  $\sigma$ , that also denotes the standard deviation. Since the Poisson distribution is a discrete distribution then all intensities lower than 1 became zeros, vanishing most of the high-frequency data components. We use the tabulation by Henke *et al.* [68] to obtain the complex refractive properties of materials at 5 keV beam energy. The object was rotated discretely at regular intervals from 0 to  $2\pi$  and shifted about 10 nm after each object rotation to form a spiral scan pattern, as previously proposed in [2].

**3.2. Approximate minimization**

In this section, we discuss the relative importance of iterating the inner gradient descent problems Eqs. (5) and (6) and the outer ADMM problem. In this experiment, the object is rotated 400 times at regular intervals from 0 to  $2\pi$  and has approximately 30% probe overlap between adjacent probe positions. Recall that if we solved subproblems Eqs. (9) and (10) exactly at every iteration,

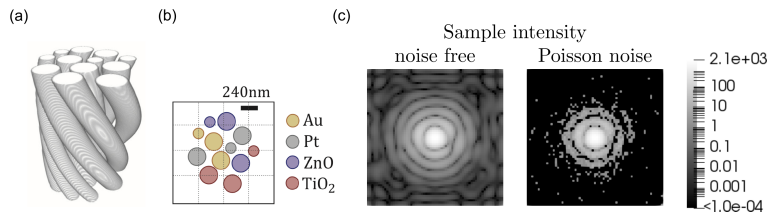


Fig. 2. (a) 3D object; (b) its 2D cross-section and the material composition; (c) samples of simulated measurement data for the noise-free and noise-added simulations with  $\sigma$ , where  $\sigma$  is the square-root of the corresponding peak intensity (standard deviation).

we would only monitor the primal residual Eq. (18) and the dual residual Eq. (19). In our simulations, we also monitor Eq. (20) and Eq. (33), which are ptychographic phase retrieval and tomography problem residuals, respectively. These residuals measure the accuracy of each subproblem at every outer iteration due to the approximate minimization. Table 1 shows the primal and dual residuals for twelve simulations at the last ADMM outer iteration where the number of inner iterations varies and the outer iteration is fixed to 40 and 200. In our simulations, we used a fixed step size for both subproblems,  $\gamma = \eta = 0.25$ . From our experiments, we observe

Table 1. Primal and dual residual values at the last ADMM outer iteration for twelve simulations with and without applying Poisson noise; see Figure 2c. P and T correspond to ptychographic phase retrieval and tomography problems, respectively. The object is rotated 400 times at regular intervals from 0 to  $2\pi$  and has approximately 30% probe overlap between adjacent probe positions.

Noise	Iterations		Primal	Dual	P	T
	inner (P/T)	outer	Residual	Residual	Residual	Residual
			norm	norm	norm	norm
free	500/500	40	1.3e-01	4.2e-01	4.2e-01	7.5e-07
free	500/500	200	1.6e-02	4.7e-02	4.7e-02	3.3e-08
free	1/200	200	2.4e-02	9.4e-02	7.5e-01	1.7e-06
free	200/1	200	1.5e-01	8.0e-02	8.0e-02	1.5e-05
free	4/4	200	1.1e-02	6.4e-02	1.5e-01	3.4e-06
free	1/1	200	4.0e-02	1.0e-01	8.1e-01	2.2e-05
Poisson	500/500	40	1.5e-01	4.6e-01	4.6e-01	1.0e-05
Poisson	500/500	200	1.6e-01	3.8e-02	3.8e-02	1.1e-05
Poisson	1/200	200	3.2e-02	1.0e-01	8.0e-01	9.6e-06
Poisson	200/1	200	1.7e-01	6.6e-02	6.6e-02	1.8e-05
Poisson	4/4	200	4.5e-02	6.5e-02	1.6e-01	1.1e-05
Poisson	1/1	200	6.5e-02	1.1e-01	8.5e-01	2.2e-05

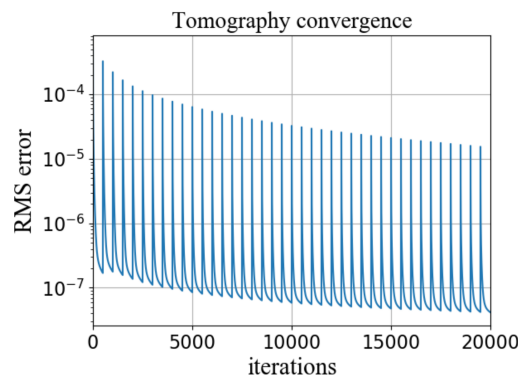


Fig. 3. Convergence plot of the reconstruction error of  $x$  from solving tomography and ptychographic phase retrieval problems using the joint approach with noise applied. The object is rotated 400 times at regular intervals from 0 to  $2\pi$  and has approximately 30% probe overlap between adjacent probe positions. The inner and outer iterations are 500 and 40, respectively. The  $l^2$  norm of the ground truth model is 1.1e-2.

that solving inner iterations to high accuracy results in minor differences in residuals while taking substantially more time.

The reason for the minor differences in ADMM convergence with high inner problem iterations is suggested in Figure 3. This figure shows the convergence of  $x$ , initialized as a zero vector, for the tomography problem across 40 outer iterations when the inner tomography iteration count is 500. While the root-mean-square (RMS) error decreases during iterations of the tomography problem, it jumps up when switching to the ptychographic phase retrieval problem. Hence, we eliminate these jumps by choosing only a few inner iterations as suggested in Table 1.

For simulations, we used our graphical processing unit (GPU) solver for ptychography and tomography problems. The total computational time on NVidia Quadro M5000 for the case with 200 outer and 500 inner iterations is approximately 65 mins.

It is known that ADMM can reach a modest accuracy even when the individual ADMM problems do not converge to optimal values [51]. In Figure 4, we demonstrate the convergence of residual plots with noise-free and noise-added simulations, respectively. Even though a higher number of inner iterations reach the stopping criteria in fewer number of outer iterations, substantially more time is required. In addition, ADMM is known to reach an acceptable solution within a few tens of outer iterations in practice [51].

### 3.3. Comparative studies

In this section, we first compared reconstructions that are obtained by using the conventional sequential and the proposed joint approach for noise-free and noise-added simulations; see Figure 5. It is important to note that  $\beta$  reconstructions are more prone to noise than are  $\delta$  reconstructions because the illumination energy is selected from the hard x-ray band. In the conventional sequential approach, we also solve the ptychography and tomography problems via the gradient descent approach. Similar to the previous simulation, we used 4 inner iterations for both the ptychographic phase retrieval and tomography problems and 50 outer iterations for the joint approach. For the conventional approach, we use 200 iterations for both the ptychographic phase retrieval and tomography problems for a fair comparison.

In this experiment, the object is first rotated 100 and then 400 times at regular intervals from 0 to  $2\pi$  and has approximately 70% probe overlap between adjacent probe positions. For noise-free simulations, the joint approach reconstructions are slightly better than the ones from the conventional approach. After reducing the probe overlap between adjacent probe positions

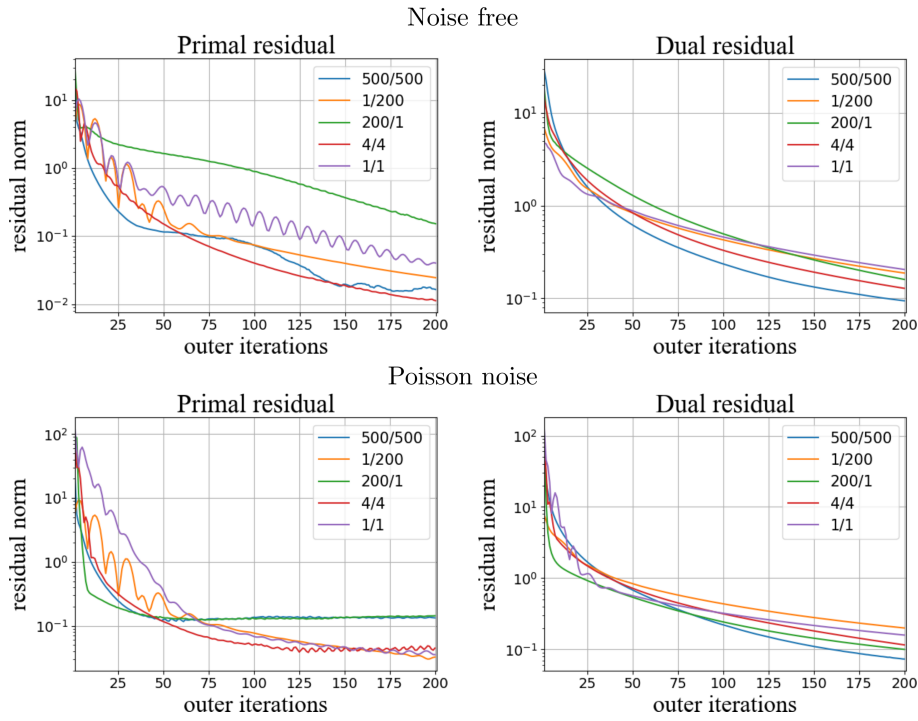


Fig. 4. The primal Eq. (18) and dual residual Eq. (19) decay values for five simulations for the noise-free model and for the model with Poisson noise. The object is rotated 400 times at regular intervals from 0 to  $2\pi$  and has approximately 30% probe overlap between adjacent probe positions. The number of inner iterations for ptychographic phase retrieval (P) and tomography (T) are shown in legends as P/T and the outer iterations is fixed to 200.

to 30% and using both 400 and 100 rotations, the deterioration of image quality for both  $\beta$  and  $\delta$  reconstructions is still visible, but the joint approach is still more accurate, see Figure 5. Moreover, when we distort data by applying Poisson noise (see Figure 2c), the reconstruction results show that the conventional sequential approach is more sensitive to noise than the joint approach. Note that the dark circle in the delta reconstruction corresponds to the global offset of the phase that can be found by adding boundary conditions to the ptychography problem.

In the following experiment, we compare the coupled approach used in [2] and our proposed joint approach. In this experiment (Fig. 6), we used the same solvers and the same number of inner and outer iterations for the ptychography and tomography problems to minimize the amplitude-based cost function for a fair comparison. The number of inner iterations is 4 for both the phase retrieval and tomography problems and the number of outer iterations is 50. For coupled approach, the number of outer iterations refers to the number of times each minimization problem solved in an alternating fashion (no dual update). Our experiments show that the coupled approach typically needs more iterations to produce a similar-error result as our joint method. In particular, for reconstructions in Figure 6, the coupled approach needs 1.2-1.5 times more iterations.

#### 4. Discussion

One of the main advantages of ADMM framework is its decomposability to two subproblems. In our proposed joint approach, these subproblems become the ptychographic phase retrieval, (8), and the conventional tomographic reconstruction problem, Eq. (9). Hence, it allows us to

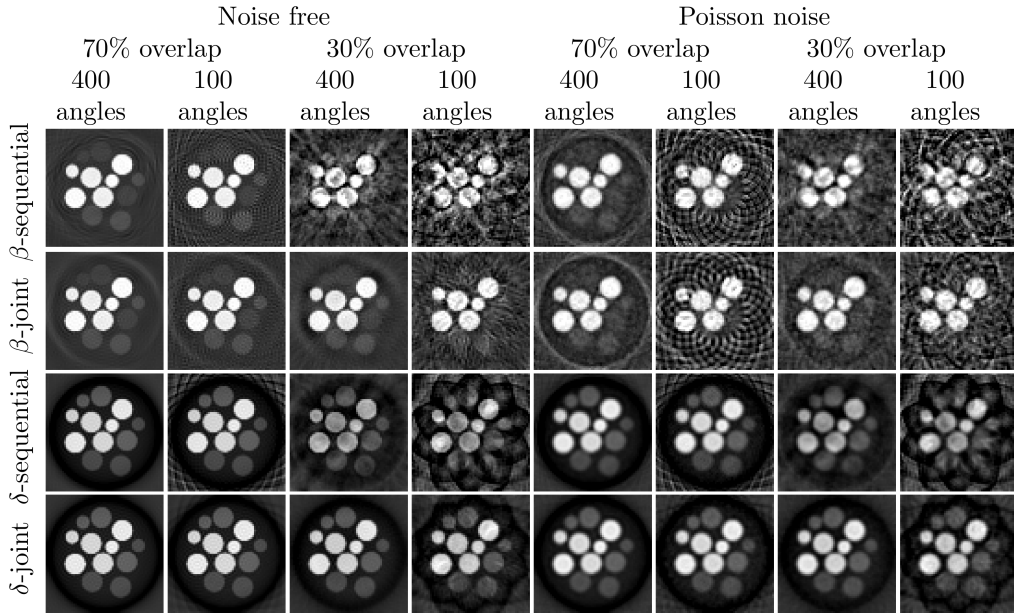


Fig. 5. Reconstructions obtained by using the conventional sequential (standard) and the proposed joint approach for noise-free and noise-added simulations with  $\sigma = 46$  (see Fig. 2c). The object is rotated 100 and 400 times at regular intervals from 0 to  $2\pi$  and has approximately 30% and 70% probe overlap between adjacent probe positions for each simulation.

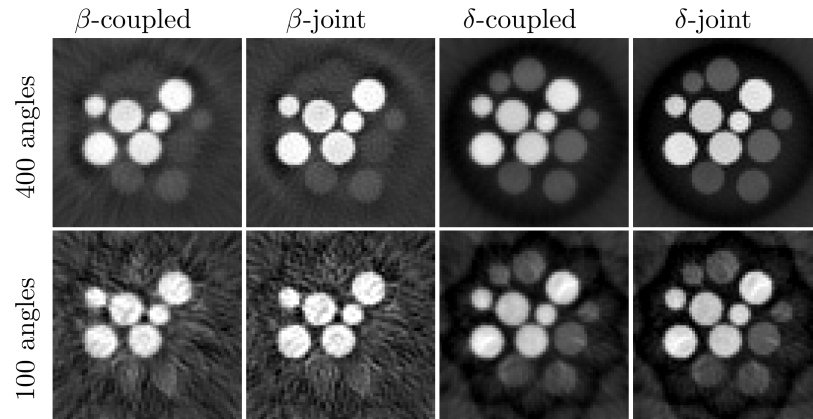


Fig. 6. Reconstructions obtained by using the coupled approach [2] and the proposed joint approach for noise-added simulations with  $\sigma = 46$  (see Fig. 2c). The object is rotated 100 and 400 times at regular intervals from 0 to  $2\pi$  and has approximately 30% probe overlap between adjacent probe positions for each simulation.

use existing state-of-the-art algorithms and their parallel implementations for each subproblem. Here we used gradient descent for both subproblems as an introduction to the framework, but optimizers may be tailored to the problems described by Eqs. (8) and (9) depending on the acquisition geometry or other factors such as noise or known sample properties.

In section 3.2, we showed that efficient updates of  $\psi_\theta$  and  $x$  make the joint approach computationally more effective. Our method to speed up ADMM was early termination in the optimization of  $\psi_\theta$  and  $x$  (Algorithm 1). Even though early termination leads to only an approximate minimization of these variables, the joint approach successfully recovers the object as we demonstrated in Figures 5 and 6. As discussed in [51], we also observed that over optimizing  $\psi_\theta$  and  $x$  can slow convergence when these problems are not well aligned. Therefore, we significantly speed up the joint approach by using only a few number of inner iterations while running ADMM for a few tens of iteration. For the same reason, we avoid using the closed form tomographic solution, which, in addition, is not robust to noise.

By jointly solving the tomography and ptychographic phase retrieval problems, we have relaxed the constraint that requires lateral probe overlap at discrete projection angles since we have naturally occurring angular overlap in a 3D acquisition setting. Thus, we can explore arbitrary scanning trajectories that are a better fit for scanning probes and may lead to faster data acquisition and greater robustness to noise [69].

We have not addressed yet the computational performance of ADMM for ptycho-tomography. The ability of our joint approach to relax data acquisition constraints creates an opportunity for reducing the computations because we do not need to have access to an entire projection in order to solve the tomography problem. For example, after a single iteration of the ptychographic phase retrieval problem, the images can directly be used to partially update the object through tomography. Therefore, we can employ in-slice parallelization techniques in tomography [70–72] since there exist a one-to-one relationship between sinograms and reconstructed slices to optimize the application runtime performance. Similarly, there are several studies for parallelization of the ptychographic phase retrieval problem [73, 74].

Another important factor is the computational complexity of the ptychography and tomography problems. Let the reconstruction domain consist of  $K^3$  voxels and  $M$  number of measured projections (i.e.,  $\psi$ ). Then, the computational complexity of the iterative reconstruction algorithms becomes  $O(MK^3)$  if the forward and adjoint tomographic operators are computed by straightforward discretization of line integrals. However in our case, the complexity is reduced to  $O(K^2 \log K + MK^2)$  since the operators are computed by a Fourier-based approach. In this way, the complexity of both ptychography and tomography problems grows at a similar rate, and is tractable. We also plan to improve the computational speed of the tomography problem by switching to log-polar coordinates [75] which demonstrates 5-10 times performance gain compared to other Fourier-based methods. These implementations will be made openly available under TomoPy, which is a library for tomographic image reconstruction [76].

Because the calculation of the DFTs is required for speeding both problems, GPUs can be well suited for both problems. However, the memory of GPUs is limited, and data transfers to and from the GPUs can become the bottleneck at runtime.

In many real-life applications of ptychography, the probe function is never fully coherent and never exactly known, so it needs to be reconstructed simultaneously with the object transfer function for obtaining satisfactory reconstructions. After the initial experimental demonstrations of simultaneous probe and object retrieval [77], modeling the probe by using the orthogonal decomposition of its mutual coherence function [78] has been widely adopted. In our ADMM framework, the probe retrieval can be included as part of Eq. (5), either by using the orthogonal decomposition method or by using a similar ADMM approach [79].

## 5. Conclusions

We have shown that using ADMM for solving the joint problem for ptycho-tomography yields better reconstructions than solving two problems sequentially because it is more robust to noise and can free restrictions on data acquisition. The ADMM framework is also generic and allows the use of different optimizers for the tomography and ptychography problems and their regularization. Besides, our approach decomposes the joint problem into two well-defined subproblems, each of which can be effectively solved through parallel computing. As no illumination overlap is necessary among laterally adjacent scan points, this technique can allow for more flexible data acquisition. It thus promises to open new avenues in design and operation of the future ptycho-tomography instruments.

## Funding

U.S. Department of Energy, Office of Science (DE-AC02-06CH11357); Swedish Research Council (2017-00583).

## References

1. W. Hoppe, "Beugung im inhomogenen primärstrahlwellenfeld, I. prinzip einer phasenmessung," *Acta Crystallogr. A* **25**, 495–501 (1969).
2. D. Gürsoy, "Direct coupling of tomography and ptychography," *Opt. Lett.* **42**, 3169–3172 (2017).
3. J. M. Rodenburg, A. C. Hurst, A. G. Cullis, B. R. Dobson, F. Pfeiffer, O. Bunk, C. David, K. Jefimovs, and I. Johnson, "Hard-x-ray lensless imaging of extended objects," *Phys. Rev. Lett.* **98**, 034801 (2007).
4. J. M. Rodenburg, A. C. Hurst, and A. G. Cullis, "Transmission microscopy without lenses for objects of unlimited size," *Ultramicroscopy* **107**, 227–231 (2007).
5. P. Thibault, M. Dierolf, A. Menzel, O. Bunk, C. David, and F. Pfeiffer, "High-resolution scanning x-ray diffraction microscopy," *Science* **321**, 379–382 (2008).
6. M. Dierolf, O. Bunk, S. Kynde, P. Thibault, I. Johnson, A. Menzel, K. Jefimovs, C. David, O. Marti, and F. Pfeiffer, "Ptychography & lensless x-ray imaging," *Europhys. News* **39**, 22–24 (2008).
7. M. Dierolf, A. Menzel, P. Thibault, P. Schneider, C. M. Kewish, R. Wepf, O. Bunk, and F. Pfeiffer, "Ptychographic x-ray computed tomography at the nanoscale," *Nature* **467**, 436–439 (2010).
8. M. Holler, J. Raabe, A. Diaz, M. Guizar-Sicairos, C. Quitmann, A. Menzel, and O. Bunk, "An instrument for 3D x-ray nano-imaging," *Rev. Sci. Instrum.* **83**, 073703 (2012).
9. A. Diaz, P. Trtik, M. Guizar-Sicairos, A. Menzel, P. Thibault, and O. Bunk, "Quantitative x-ray phase nanotomography," *Phys. Rev. B* **85**, 020104 (2012).
10. K. Giewekemeyera, P. Thibault, S. Kalbfleisch, A. Beerlinka, C. M. Kewishc, M. Dierolf, F. Pfeiffer, and T. Salditt, "Quantitative biological imaging by ptychographic x-ray diffraction microscopy," *PNAS* **107**, 529–534 (2009).
11. R. N. Wilke, M. Priebe, M. Bartels, K. Giewekemeyer, A. Diaz, P. Karvinen, and T. Salditt, "Hard x-ray imaging of bacterial cells: nano-diffraction and ptychographic reconstruction," *Opt. Express* **20**, 19232–19254 (2012).
12. E. Lima, A. Diaz, M. Guizar-Sicairos, S. Gorelick, P. Pernot, T. Schleirer, and A. Menzel, "Cryo-scanning x-ray diffraction microscopy of frozen-hydrated yeast," *J. Microsc.* **249**, 1–7 (2013).
13. A. Diaz, B. Malkova, M. Holler, M. Guizar-Sicairos, E. Lima, V. Panneels, G. Pigino, A. G. Bittermann, L. Wettstein, T. Tomizaki, O. Bunk, G. Schertler, T. Ishikawa, R. Wepf, and A. Menzel, "Three-dimensional mass density mapping of cellular ultrastructure by ptychographic x-ray nanotomography," *J. Struct. Biol.* **192**, 461–469 (2015).
14. J. Deng, Y. S. G. Nashed, S. Chen, N. W. Phillips, T. Peterka, R. Ross, S. Vogt, C. Jacobsen, and D. J. Vine, "Continuous motion scan ptychography: characterization for increased speed in coherent x-ray imaging," *Opt. Express* **23**, 5438 (2015).
15. A. Schropp, P. Boye, A. Goldschmidt, S. Honig, R. Hoppe, J. Patommel, C. Rakete, D. Samberg, S. Stephan, S. Schoder, M. Burghammer, and C. G. Schroer, "Non-destructive and quantitative imaging of a nano-structured microchip by ptychographic hard x-ray scanning microscopy," *J. Microsc.* **241**, 9–12 (2011).
16. B. Mike, S. Tobias, G. Thomas, R. Michael, G. Klaus, G. Sophie-Charlotte, S. Tim, and R. Axel, "Chemical contrast in soft x-ray ptychography," *Phys. Rev. Lett.* **107**, 208101 (2011).
17. C. L. Hoy, N. J. Durr, and A. Ben-Yakar, "Fast-updating and nonrepeating Lissajous image reconstruction method for capturing increased dynamic information," *Appl. Opt.* **50**, 2376–2382 (2011).
18. P. Trtik, A. Diaz, M. Guizar-Sicairos, A. Menzel, and O. Bunk, "Density mapping of hardened cement paste using ptychographic x-ray computed tomography," *Cem. & Concr. Compos.* **36**, 71–77 (2013).
19. B. Chen, M. Guizar-Sicairos, G. Xiong, L. Shemilt, A. Diaz, J. Nutter, N. Burdet, S. Huo, J. Mancuso, A. Monteith, F. Vergeer, A. Burgess, and I. Robinson, "Three-dimensional structure analysis and percolation properties of a barrier marine coating," *Sci. Rep.* **3**, 1177 (2013).

20. M. Holler, A. Diaz, M. Guizar-Sicairos, P. Karvinen, E. Färm, E. Härkönen, M. Ritala, A. Menzel, J. Raabe, and O. Bunk, "X-ray ptychographic computed tomography at 16 nm isotropic 3D resolution," *Sci. Reports* **4**, 3857 (2014).
21. K. Høydalsvik, J. B. Fløystad, T. Zhao, M. Esmaeili, A. Diaz, J. W. Andreasen, R. H. Mathiesen, M. Rønning, and D. W. Breiby, "In situ x-ray ptychography imaging of high-temperature CO<sub>2</sub> acceptor particle agglomerates," *Appl. Phys. Lett.* **104**, 241909 (2014).
22. J. N. Weker and M. F. Toney, "Emerging in situ and operando nanoscale x-ray imaging techniques for energy storage materials," *Adv. Funct. Mater.* **25**, 1622–1637 (2015).
23. J. Deng, D. J. Vine, S. Chen, Y. S. G. Nashed, Q. Jin, N. W. Phillips, T. Peterka, R. Ross, S. Vogt, and C. J. Jacobsen, "Simultaneous cryo x-ray ptychographic and fluorescence microscopy of green algae," *PNAS* **112**, 2314–2319 (2015).
24. M. W. M. Jones, K. D. Elgass, M. D. Junker, M. D. de Jonge, and G. A. van Riessen, "Molar concentration from sequential 2-D water-window x-ray ptychography and x-ray fluorescence in hydrated cells," *Sci. Rep.* **6**, 24280 (2016).
25. M. Holler, M. Guizar-Sicairos, E. H. R. Tsai, R. Dinapoli, E. Müller, O. Bunk, J. Raabe, and G. Aepli, "High-resolution non-destructive three-dimensional imaging of integrated circuits," *Nature* **543**, 402–406 (2017).
26. J. Deng, Y. P. Hong, S. Chen, Y. S. G. Nashed, T. Peterka, A. J. F. Levi, J. Damoulakis, S. Saha, T. Eiles, and C. Jacobsen, "Nanoscale x-ray imaging of circuit features without wafer etching," *Phys. Rev. B* **95**, 104111 (2017).
27. F. Pfeiffer, "X-ray ptychography," *Nat. Photonics* **12**, 9–17 (2018).
28. R. W. Gerchberg and W. O. Saxton, "A practical algorithm for the determination of phase from image and diffraction plane pictures," *Optik* **35**, 237–246 (1972).
29. J. R. Fienup, "Reconstruction of an object from the modulus of its Fourier transform," *Opt. Lett.* **3**, 27–29 (1978).
30. J. R. Fienup, "Phase retrieval algorithms: a comparison," *Appl. Opt.* **21**, 2758–2769 (1982).
31. M. Guizar-Sicairos and J. R. Fienup, "Phase retrieval with transverse translation diversity: a nonlinear optimization approach," *Opt. Express* **16**, 7264–7278 (2008).
32. V. Elser, "Phase retrieval by iterated projections," *J. Opt. Soc. Am. A* **20**, 40–55 (2003).
33. J. M. Rodenburg and H. M. L. Faulkner, "A phase retrieval algorithm for shifting illumination," *Appl. Phys. Lett.* **85**, 4795–4797 (2004).
34. Z. Wen, C. Yang, X. Liu, and S. Marchesini, "Alternating direction methods for classical and ptychographic phase retrieval," *Inverse Probl.* **28**, 115010 (2012).
35. P. Thibault and M. Guizar-Sicairos, "Maximum-likelihood refinement for coherent diffractive imaging," *New J. Phys.* **14**, 063004 (2012).
36. E. J. Candès, Y. C. Eldar, T. Strohmer, and V. Voroninski, "Phase retrieval via matrix completion," *SIAM J. on Imaging Sci.* **6**, 199–225 (2013).
37. S. Marchesini, A. Schirozek, C. Yang, H. Wu, and F. Maia, "Augmented projections for ptychographic imaging," *Inverse Probl.* **29**, 115009 (2013).
38. J. Bolte, S. Sabach, and M. Teboulle, "Proximal alternating linearized minimization for nonconvex and nonsmooth problems," *Math. Program.* **146**, 459–494 (2014).
39. E. J. Candès, X. Li, and M. Soltanolkotabi, "Phase retrieval via Wirtinger flow: theory and algorithms," *IEEE Transactions on Inf. Theory* **61**, 1985–2007 (2015).
40. R. Hesse, D. R. Luke, S. Sabach, and M. K. Tam, "Proximal heterogeneous block implicit-explicit method and application to blind ptychographic diffraction imaging," *SIAM J. on Imaging Sci.* **8**, 426–457 (2015).
41. L. Bian, J. Suo, G. Zheng, K. Guo, F. Chen, and Q. Dai, "Fourier ptychographic reconstruction using Wirtinger flow optimization," *Opt. Express* **23**, 4856–4866 (2015).
42. A. Maiden, D. Johnson, and P. Li, "Further improvements to the ptychographical iterative engine," *Optica* **4**, 736–745 (2017).
43. P. Li and A. M. Maiden, "Ten implementations of ptychography," *J. Microsc.* **269**, 187–194 (2018).
44. H. Chang, Y. Lou, Y. Duan, and S. Marchesini, "Total variation-based phase retrieval for Poisson noise removal," *SIAM J. on Imaging Sci.* **11**, 24–55 (2018).
45. H. Chang, S. Marchesini, Y. Lou, and T. Zeng, "Variational phase retrieval with globally convergent preconditioned proximal algorithm," *SIAM J. on Imaging Sci.* **11**, 56–93 (2018).
46. T. Ramos, B. E. Grönager, M. S. Andersen, and J. W. Andreasen, "Direct 3D tomographic reconstruction and phase-retrieval of far-field coherent diffraction patterns," *arXiv preprint arXiv:1808.02109* (2018).
47. P. Li and A. Maiden, "Multi-slice ptychographic tomography," *Sci. Reports* **8**, 2049 (2018).
48. M. A. Gilles, Y. S. G. Nashed, C. J. M. Du, and S. M. Wild, "3D x-ray imaging of continuous objects beyond the depth of focus limit," *Optica* **5**, 1078–1086 (2018).
49. K. Shimomura, M. Hirose, T. Higashino, and Y. Takahashi, "Three-dimensional iterative multislice reconstruction for ptychographic x-ray computed tomography," *Opt. Exp.* **26**, 31199 (2018).
50. H. Öztürk, H. Yan, Y. He, M. Ge, Z. Dong, M. Lin, E. Nazaretski, I. K. Robinson, Y. S. Chu, and X. Huang, "Multi-slice ptychography with large numerical aperture multilayer laue lenses," *Optica* **5**, 601 (2018).
51. S. Boyd, N. Parikh, E. Chu, B. Peleato, and J. Eckstein, "Distributed optimization and statistical learning via the alternating direction method of multipliers," *Foundations Trends Mach. Learn.* **3**, 1–122 (2011).
52. R. Glowinski and A. Marroco, "Sur l'approximation, par éléments finis d'ordre un, et la résolution, par pénalisation-dualité d'une classe de problèmes de Dirichlet non linéaires," *RAIRO Anal. Numer.* **9**, 41–76 (1975).
53. D. Gabay and B. Mercier, "A dual algorithm for the solution of nonlinear variational problems via finite element

- approximation," *Optik* **2**, 17–40 (1976).
54. B. He and X. Yuan, "On the O(1/n) convergence rate of the Douglas-Rachford alternating direction method," *SIAM J. Numer. Anal.* **50**, 700–709 (2012).
  55. M. Hong, Z. Luo, and M. Razaviyayn, "Convergence analysis of alternating direction method of multipliers for a family of nonconvex problems," *SIAM J. on Optim.* **26**, 337–364 (2016).
  56. Y. Wang, W. Yin, and J. Zeng, "Global convergence of ADMM in nonconvex nonsmooth optimization," *J. Sci. Comput.* **78**, 29–63 (2019).
  57. D. Davis and W. Yin, "Convergence rate analysis of several splitting schemes," in *Splitting Methods in Communication, Imaging, Science, and Engineering*, R. Glowinski, S. J. Osher, and W. Yin, eds. (Springer International Publishing, Cham, 2016), pp. 115–163.
  58. C. Yang, J. Qian, A. Schirozek, F. Maia, and S. Marchesini, "Iterative algorithms for ptychographic phase retrieval," arXiv preprint arXiv:1105.5628 (2011).
  59. L.-H. Yeh, J. Dong, J. Zhong, L. Tian, M. Chen, G. Tang, M. Soltanolkotabi, and L. Waller, "Experimental robustness of Fourier ptychography phase retrieval algorithms," *Opt. Express* **23**, 33214–33240 (2015).
  60. J. Douglas and H. H. Rachford, "On the numerical solution of heat conduction problems in two and three space variables," *Transactions Am. Math. Soc.* **82**, 421–439 (1956).
  61. M. R. Hestenes, "Multiplier and gradient methods," *J. Optim. Theory Appl.* **4**, 303–320 (1969).
  62. M. J. Powell, "A method for nonlinear constraints in minimization problems," *Optimization* pp. 283–298 (1969).
  63. L. Li, X. Wang, and G. Wang, "Alternating direction method of multipliers for separable convex optimization of real functions in complex variables," *Math. Probl. Eng.* **2015**, 104531 (2015).
  64. R. Remmert, *Theory of Complex Functions* (Springer, 1991).
  65. K. Kreutz-Delgado, "The complex gradient operator and the CR-calculus," arXiv preprint arXiv:0906.4835 (2009).
  66. G. Beylkin, "On the fast Fourier transform of functions with singularities," *Appl. Comput. Harmon. Analysis* **2**, 363–381 (1995).
  67. D. J. Ching and D. Gürsoy, "XDesign: an open-source software package for designing x-ray imaging phantoms and experiments," *J. synchrotron radiation* **24**, 537–544 (2017).
  68. B. L. Henke, E. M. Gullikson, and J. C. Davis, "X-ray interactions: photoabsorption, scattering, transmission, and reflection at  $E=50\text{--}30,000\text{ eV}$ ,  $Z=1\text{--}92$ ," *At. Data Nucl. Data Tables* **54**, 181–342 (1993).
  69. D. J. Ching, M. Hidayetoğlu, T. Bicer, and D. Gürsoy, "Rotation-as-fast-axis scanning-probe x-ray tomography: the importance of angular diversity for fly-scan modes," *Appl. Opt.* **57**, 8780–8789 (2018).
  70. T. Bicer, D. Gürsoy, R. Kettimuthu, I. T. Foster, B. Ren, V. D. Andrade, and F. De Carlo, "Real-time data analysis and autonomous steering of synchrotron light source experiments," in *2017 IEEE 13th International Conference on e-Science*, (2017), pp. 59–68.
  71. T. Bicer, D. Gürsoy, V. D. Andrade, R. Kettimuthu, W. Scullin, F. D. Carlo, and I. T. Foster, "Trace: a high-throughput tomographic reconstruction engine for large-scale datasets," *Adv. Struct. Chem. Imaging* **3**, 6 (2017).
  72. T. Bicer, D. Gürsoy, R. Kettimuthu, F. De Carlo, G. Agrawal, and I. T. Foster, "Rapid tomographic image reconstruction via large-scale parallelization," in *Euro-Par 2015: Parallel Processing*, J. L. Träff, S. Hunold, and F. Versaci, eds. (Springer, Berlin, Heidelberg, 2015), pp. 289–302.
  73. Y. S. G. Nashed, D. J. Vine, T. Peterka, J. Deng, R. Ross, , and C. Jacobsen, "Parallel ptychographic reconstruction," *Opt. Express* **2**, 32082–32097 (2014).
  74. S. Marchesini, H. Krishnan, B. J. Daumer, D. A. Shapiro, T. Perciano, J. A. Sethian, and F. R. N. C. Maia, "SHARP: a distributed GPU-based ptychographic solver," *J. Appl. Cryst.* **49**, 1245–1252 (2016).
  75. F. Andersson, M. Carlsson, and V. V. Nikitin, "Fast algorithms and efficient GPU implementations for the Radon transform and the back-projection operator represented as convolution operators," *SIAM J. on Imaging Sci.* **9**, 637–664 (2016).
  76. D. Gürsoy, X. Xiao, F. D. Carlo, and C. Jacobsen, "Tomopy: a framework for the analysis of synchrotron tomographic data," *J. Synchrotron Rad.* **21**, 1188–1193 (2014).
  77. P. Thibault, M. Dierolf, O. Bunk, A. Menzel, and F. Pfeiffer, "Probe retrieval in ptychographic coherent diffractive imaging," *Ultramicroscopy* **109**, 338–343 (2009).
  78. E. Wolf, "New theory of partial coherence in the space-frequency domain. Part I: spectra and cross spectra of steady-state sources," *JOSA* **72**, 343–351 (1982).
  79. H. Chang, P. Enfedaque, Y. Lou, and S. Marchesini, "Partially coherent ptychography by gradient decomposition of the probe," *Acta Crystallogr. Sect. A: Foundations Adv.* **74**, 157–169 (2018).